Enhanced mechanical strength and electrical conductivity of Al-Ni-based conductor cast alloys containing Mg and Si

Ahmed Y. Algendy [1, *], Mousa Javidani[1], Siamak Nikzad Khangholi[1], Lei Pan[2] and X.-Grant Chen [1,*]

[1] Department of Applied Science, University of Quebec at Chicoutimi, Saguenay (QC), G7H 2B1, Canada

[2] Arvida Research and Development Center, Rio Tinto Aluminum, Saguenay (QC), G7S 4K8, Canada

* Corresponding authors: aalgendy@etu.uqac.ca, xgrant_chen@uqac.ca.

Abstract

The electrical conductivity (EC), mechanical strength, hot tearing susceptibility (HTS), and related microstructure of Al–xNi–0.55Mg–0.55Si conductor alloys (x = 1–4 wt%) are investigated. Adding Mg and Si into Al–Ni-based alloys, numerous β''/β' precipitate after T5 and T6 treatments, thus significantly improving the EC and mechanical strength. The HTS of the alloys reduces significantly as the Ni content increases, mainly because of an increase in the eutectic Al–Al3Ni and a reduction in the grain size. Under T5 condition, the tensile strengths increase gradually with the Ni content and reach a medium strength level, with yield strength (YS) of 158–205 MPa and EC of 47.1–50.7% IACS. After applying T6, all alloys achieve a high strength, with YS of 246–287 MPa and EC of 47.7–51.1% IACS. However, the strength decreases with increasing Ni content. In general, the Al3Ni–0.55Mg–0.55Si alloy presents a better trade-off among HTS, YS, and EC among the four alloys investigated. Due to its excellent properties (EC of 49.4% IACS and YS of 178 MPa in T5, and EC of 49.7% IACS and YS of 250 MPa in T6), the Al3Ni–0.55Mg–0.55Si alloy is a promising material for the fabrication of Al conductor cast alloys.

Keywords: Al-Ni-based conductor alloys, Mechanical strength, Electrical conductivity, T5 and T6 heat treatment, Hot tearing susceptibility.

1 Introduction

In recent years, the demand for high-strength castable aluminum conductor alloys has increased rapidly in various industrial sectors [1, 2]. One of the main applications of Al-based conductors is the fabrication of various automotive components, such as rotors, stators, and busbars, in electric and hybrid vehicles [3], in which good castability with high electrical conductivity (EC) and high mechanical strength are essential. It is reported that the castable Al-based conductor alloys require a minimum yield strength (YS) of 90 MPa and an EC of 48% IACS [3]. Al-Si-, Al-Fe-, and Al-Ni-based alloy systems are the principal cast alloys investigated for the development of high-strength conductor products [2-4].

Al-Si-based alloys (typically A365) are commonly used in automotive cast components owing to their excellent castability and high mechanical strength (YS $\geq$ 175 MPa). However, these Al alloys present a low EC ($\leq$ 40% IACS) [5], which renders them less suitable as conductor alloys. Al-Fe-based alloys exhibit excellent castability with high EC ($\sim$ 53% IACS), but at the expense of low mechanical strength [2, 5]. Recently, several studies have been conducted to identify alternative alloy systems to Al-Si based alloys for castable Al conductor alloys [4-7]. Kotiadis et al. and Kim et al. [4, 5] investigated the effect of Ni addition in Al-Fe-based alloys for high-conductivity applications. Koutsoukis et al. [5] investigated Al-Ni, Al-Fe, and Al-Fe-Ni eutectic systems as castable conductor alloys. Breton et al. [8] investigated the effect of adding Si and Mg on the mechanical properties and EC of an Al2Ni alloy and reported promising results, i.e., a YS of 150–225 MPa and an EC of 46%–48% IACS after T6 heat treatment. Among the alloys investigated, Al-Ni-based alloys have recently received increasing attention owing to their excellent EC, castability, and strength [3]. However, Al-Ni-based alloys generally exhibit unsatisfactory mechanical strengths owing to the limited contribution of Ni in alloy strengthening, either as a solid solution or precipitation hardening [4, 5].

The main challenge in developing a high-strength castable Al conductor alloy is the mutually exclusive nature of the electrical and mechanical properties, i.e., the mechanisms that improve the strength deteriorate the EC, and vice versa. The principal strengthening mechanisms of Al-cast alloys include solid solution, grain boundary, and precipitation strengthening. The EC is dominated by the movement of valence electrons; thus, any disturbance in the Al lattice periodicity resulting from defects in the crystal structure (e.g., vacancies, solute atoms, and grain boundaries) reduces the EC [9-13]. However, the adverse effect of the strengthening mechanisms on the EC varies depending on their impact on the distortion of the α-Al crystal structure. For instance, alloying elements in the solid solution are the most deleterious to the EC; however, transforming the solute atoms to precipitates can mitigate the distortion of Al lattice, thus improving the EC [11, 12, 14]. In addition, fine nanosized precipitates are more beneficial to strengthening than solute atoms.

Adding Ni to Al results in various intermetallic phases, including Al_3Ni, Al_3Ni_2, $AlNi$, Al_3Ni_5, and $AlNi_3$, based on the Al-Ni binary phase diagram [15-17]. However, the chemical composition, morphology, and amount of these intermetallic phases depend significantly on the Ni content and solidification rate [18, 19]. Studies [7, 20] showed that adding Ni into Al-0.5Fe-Mg-Zn-xNi alloys

resulted in Al₉FeNi or Al₃Ni secondary phases during solidification, and that the volume fraction of these intermetallic compounds (IMCs) increased significantly with the Ni content [7, 20]. Liu et al. [1] reported that adding Ni into an Al-Zn-Mg-Cu system increased the volume fraction of Al₃Ni IMCs without any phase formation with Zn, Mg, and Cu.

Hot tearing is one of the most deleterious defects in Al cast alloys during casting and solidification. Hot tearing susceptibility (HTS) is affected by various factors, such as alloy chemistry, casting parameters, solidification interval [21-25], grain refining [22, 25-28], residual liquid at the later stage of solidification [22, 25], and the formation of secondary phases during solidification [1, 7, 29, 30]. Liu et al. [1] reported that adding Ni into an Al-Zn-Mg-Cu-xNi alloy significantly reduced the HTS, which was attributed to the reduced vulnerabile region during solidification, a lower cracking susceptibility coefficient, and a higher amount of eutectic Al₃Ni. By contrast, Kim et al. [7] discovered that adding Ni to Al-Fe-Mg-Zn-xNi alloys increased the HTS owing to the increased interference of secondary phases in metal feeding. Cho et al. [20] showed that adding up to 0.5 wt.% Ni to an Al-Si-Fe-based alloy improved the fluidity and reduced the HTS; however, by further increasing the Ni content to 1 wt.%, the HTS elevated. These studies show different results regarding the effect of Ni on the castability of Al cast alloys in different alloy systems. To the best of the authors' knowledge, the effects of Ni, Mg, and Si on the comprehensive properties (in terms of the strength, EC, and castability) of castable Al conductor alloys are rarely investigated.

The aim of the present study is to investigate the effects of various Ni contents (1–4 wt.%) on the mechanical strength, EC, and HTS of Al-Ni-Mg-Si alloy in as-cast, T5, and T6 conditions. Optical microscopy (OM), scanning electron microscopy (SEM) with energy-dispersive X-ray spectrometry (EDS), and transmission electron microscopy (TEM) are employed to characterize the as-cast and heat-treated microstructures. Furthermore, the EC, microhardness, and tensile properties are evaluated during heat treatment. The HTS of the newly designed alloys is evaluated using a constrained rod casting (CRC) mold and via thermodynamic simulation based on the model of Hu et al. [31].

2   Experimental procedure

Four Al-Ni-based cast alloys were prepared, in which the Ni content varied from 1% to 4% and the Mg and Si levels were maintained constant. The actual chemical compositions of the experimental alloys were analyzed using optical emission spectrometry, and the results are listed in **Table 1**. The alloy designation is based on the Ni content. Commercial pure Al (99.7%), Mg (99.8%), Al-20%Ni, and Al-50%Si master alloys were used for batching the casting (all the alloy compositions used in this study are given in wt.%). The materials were melted in a graphite crucible placed in an electrical resistance furnace. The melting temperature was maintained at 780 °C for 30 min; subsequently, Ar degassing was performed for 15 min. The melt was poured into a copper permanent mold preheated at 400 °C, which had a cooling rate of 18 ºC/s to obtain thin-wall cast plates measuring 110 mm × 110 mm × 4 mm. The copper mold has been chosen to simulate the high pressure die casting conditions. The pouring temperature was adjusted to 90 °C above the liquidus temperature of each alloy.

Table 1. Chemical compositions of the experimental alloys (wt.%)

Alloys	Ni	Mg	Si	Fe	Ti	B	Al
Al1Ni	**1.09**	0.56	0.63	0.08	0.03	0.008	Bal.
Al2Ni	**2.22**	0.62	0.65	0.08	0.025	0.004	Bal.
Al3Ni	**3.16**	0.58	0.56	0.08	0.023	0.005	Bal.
Al4Ni	**4.33**	0.64	0.56	0.08	0.016	0.003	Bal.

The cast plates were subjected to two heat treatments (T5 and T6), the details of which are shown in **Figure 1**. In the T5 heat treatment, the cast components were directly aged at 180 °C for various durations (Figure 1a). The T6 heat treatment involved a solution treatment at 520 °C for 2 h, followed by water quenching and artificial aging at 180 °C for different durations (Figure 1b).
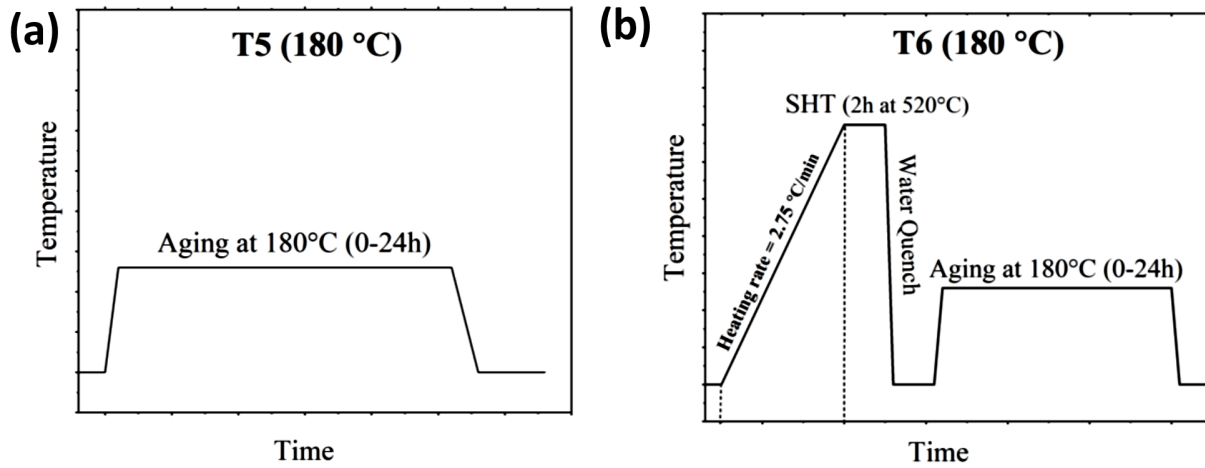
Figure 1. Illustration of (a) T5 and (b) T6 heat treatments.

The mechanical properties of the alloys were evaluated via hardness and tensile tests. The Vickers microhardness was measured at a constant load of 25 g and a dwell time of 20 s. The reported hardness values were based on the average of at least 15 measurements. Tensile testing was performed using a uniaxial tensile-testing machine (Instron 8801 servo-hydraulic unit) at a strain rate of 0.5 mm/min at 25 °C. The tensile samples were machined based on ASTM E8/E8M-16 standard, and featured a gauge length of 32 mm and a cross-sectional area of 3 mm × 6 mm. Four tensile tests were conducted in each condition to obtain the average values. EC was measured using a Sigmascope SMP 10 device based on ASTM E1004. At least 20 measurements were recorded, and the average EC was obtained.

The samples for microstructural observations were prepared using standard metallographic procedures. The grain structure was observed via OM (Nikon, Eclipse ME600) under polarized light after electro-etching using Barker's agent (3 vol.% HBF4 solution at 20 V for 2 min). The average grain size of the electro-etched samples was evaluated via the linear intercept method based on ASTM E112–12 using ImageJ software. A scanning electron microscope (JSM-6480LV)

equipped with an energy-dispersive X-ray spectrometer was used to identify the intermetallic components. The precipitates were characterized using TEM (JEM2100). For TEM analysis, samples were mechanically ground and then electropolished using a twin jet unit with 30% HNO_3 in methanol at a temperature of -25 °C. The foil thickness was measured using convergent beam electron diffraction [32]. All TEM images were obtained along the $[001]_{Al}$ zone axis.

HTS was evaluated using a CRC mold **(Figure 2)**. The CRC mold casting was performed at an angle of 17.5°. The mold cavity allowed the casting of four rods with a diameter of 9 mm and lengths of 30 (A), 65 (B), 100 (C), and 140 (D) mm. The CRC mold was preheated to 250 °C. The pouring temperature of the melt was adjusted to 70 °C above the liquidus temperature of each alloy. The casting was removed from the mold 3 min after pouring. Ten castings were performed for each alloy to obtain the average HTS values. The HTS was measured using the method described in [33].

Figure 2. Constrained rod casting (CRC) mold used in the current study.

3 Results

3.1 Electrical and mechanical properties

Figures 3(a, b) show the evolution of EC as a function of aging time under the T5 and T6 conditions. Prior to the heat treatment (0 h as-cast condition), the EC of the alloys with low Ni contents (Ni ≤ 3%) was significantly higher than that of the alloy containing 4% Ni. For instance, the EC of Al1Ni was 48.5% IACS, which reduced to 44% IACS by increasing the Ni content to 4% (Fig. 3a); this result is consistent with the results reported previously by other researchers [3, 7]. In the T5 treatment, the EC increased gradually with the aging time. Under the T6 condition (Fig. 3b), the EC increased rapidly in the early aging stage (up to 12 h); as the aging time increased, the

EC improved slightly. Up to 24 h, the EC reached values similar to those in the T5 condition. In general, the lower the Ni content of the alloys, the higher was the EC under all conditions. The EC after T5 and T6 increased significantly because most of the solute atoms precipitated out to form nanosized precipitates [12, 14, 34, 35]. It is noted that the Al2Ni and Al3Ni alloys showed a similar EC behavior (Fig. 3a-b), though the Al3Ni alloy has a higher Ni value than Al2Ni alloy. This could be correlated to the slightly higher Mg and Si contents in Al2Ni alloy relative to Al3Ni alloy, causing the slightly higher electrical resistivity [14]. Therefore, it resulted in a similar EC behavior in these two alloys.

Figures 3(c, d) show the microhardness curves during the T5 and T6 treatments. Under the T5 condition (Fig. 3c), the investigated alloys reached their peak hardness after 12 h of aging. All the investigated alloys (regardless of the Ni content) exhibited similar peak hardness values after T5 (60–62 HV). Under the T6 condition (Fig. 3d), the Al1Ni, Al2Ni, and Al3Ni alloys reached their peak hardness after 7 h; subsequently, the HV values remained almost constant. However, alloy Al4Ni reached its peak hardness after 10 h of aging (98 HV), and as the aging time increased to 24 h, its HV decreased gradually to 85 HV. The four investigated alloys achieved peak hardness values with the range of 95–99 HV under the T6 condition, which were approximately 35 HV higher than the peak hardness values under the T5 condition.
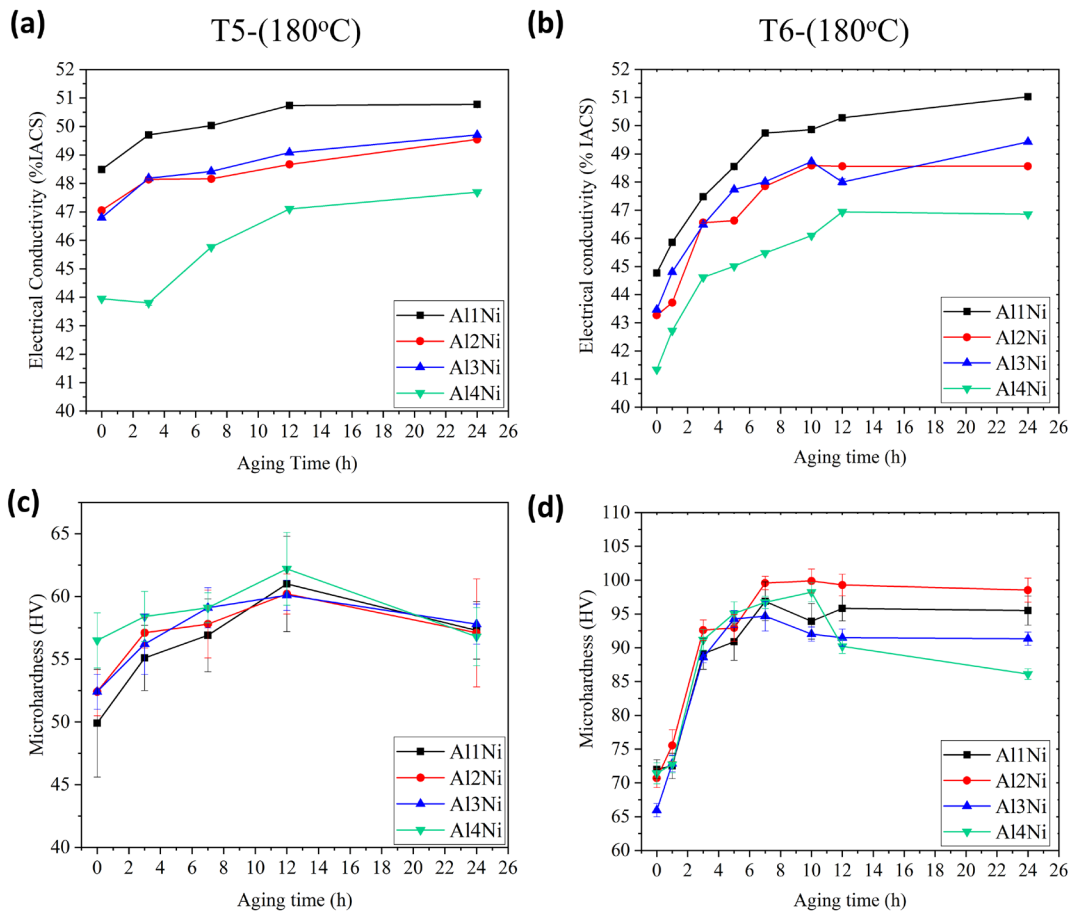
Figure 3. Evolution of electrical conductivity (a,b) and microhardness (c,d) as a function of aging time under T5 (a,c) and T6 (b,d) conditions.

Figure 4 shows the HV vs. EC at all aging times under the T5 (Figure 4a) and T6 (Figure 4b) conditions. The HV and EC values for each aging time are shown in the HV vs. EC plots. Under T5 performed at 180 °C/12 h (Figure 4a), the Al1Ni alloy exhibited the best combination of EC (51% IACS) and HV (61.1) among all the investigated alloys. As aging progressed to 24 h (Figure 3), the HV decreased considerably, with no remarkable improvement in the EC. Under the same aging conditions, the Al4Ni alloy presented the highest HV value (62.2) and the lowest EC value (47.1% IACS). Increasing the aging time to 24 h slightly improved the EC (47.7%) and significantly decreased the HV (56.6). In the T6 condition (Figure 4b), although all the investigated alloys exhibited similar peak hardness values, the Al1Ni alloy presented the best balance between HV (96.8) and EC (49.9% IACS). As aging progressed, the Al1Ni, Al2Ni, and Al3Ni alloys showed further improvement in the EC with a slight decrease in the HV, except for the Al4Ni alloy, which showed a significant decrease in the HV.
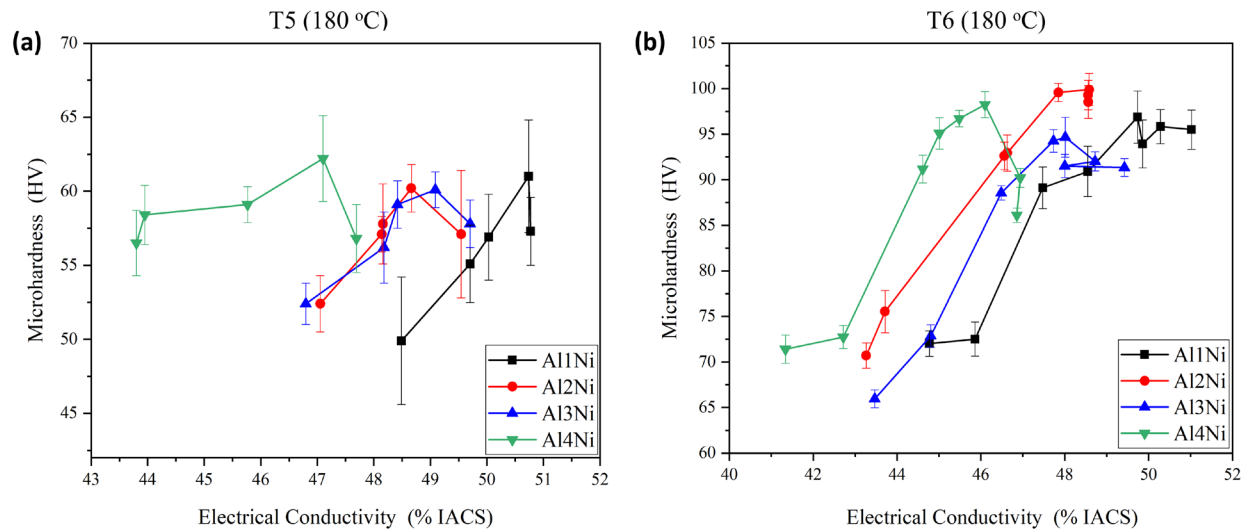

Figure 4. HV hardness as a function of EC for all aging times: (a) T5 and (b) T6 conditions.

Based on the HV and EC results shown in Figure 4, samples subjected to T5 aging (180 °C/12 h) and T6 aging (180 °C/24 h) were selected for mechanical tensile tests, and the results are presented in **Figure 5**. As shown, the evolution of the tensile strengths under the T5 and T6 conditions differed as the Ni content in the alloys increased. At T5, the higher Ni content resulted in higher YS and ultimate tensile strength (UTS) values. For instance, by increasing the Ni content from 1% to 4%, the YS and UTS for T5 increased by 30% and 27%, respectively. However, in the T6 condition, the opposite trend was observed, i.e., the higher the Ni content, the lower were the YS and UTS values. For instance, the YS and UTS decreased from 288 and 302 MPa in Al1Ni to 246 and 259 MPa in Al4Ni, which corresponds to a reduction by ~15%. The alloys subjected to T6 exhibited considerably higher tensile strengths than those subjected to T5. Figure 5b shows the

YS as a function of EC for the four investigated alloys under the T5 and T6 conditions. As shown, a lower Ni content resulted in a higher EC but a lower YS under the T5 condition. Meanwhile, a lower Ni content resulted in a higher YS under the T6 condition. The Al1Ni alloy exhibited the highest YS (288 MPa) and EC (50.7% IACS) among the four investigated alloys. The YS and EC values of the Al2Ni and Al3Ni alloys were similar.
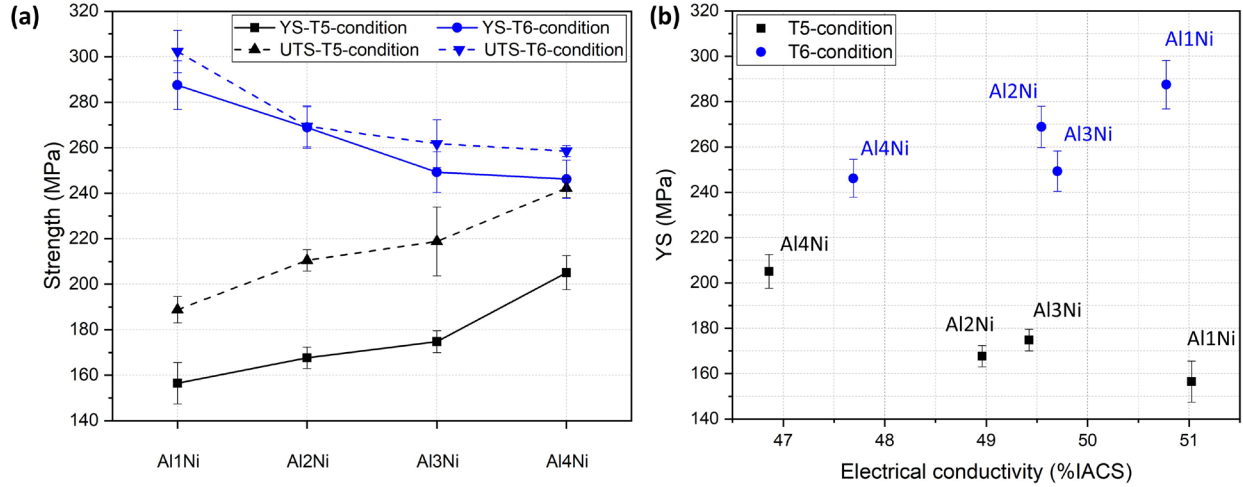

Figure 5. Evolution of (a) tensile properties and (b) YS as a function of EC after T5 aging (180 °C/12 h) and T6 aging (180 °C/24 h) conditions.

3.2 Evolution of the microstructure and phase formation

3.2.1 As-cast microstructure

The typical grain structures of the four alloys are presented in **Figures 6(a)–(d)**, and their average grain size as a function of Ni content is depicted in Figure 6e. All alloys comprised equiaxed dendritic grains of α-Al. The grain size decreased from 73.5 μm in the Al1Ni alloy to 55 μm in the Al3Ni and Al4Ni alloys, which corresponds to a reduction by 25%, by increasing the Ni content from 1% to 3%–4%, owing to the increase of the growth restriction factor with Ni addition [36]. Owing to the increased eutectic content in the high-Ni alloys, the eutectic Al-Al$_3$Ni structure surrounding the equiaxed-Al grains became visible in the Al3Ni and Al4Ni alloys, as shown in Figures 6(c, d).
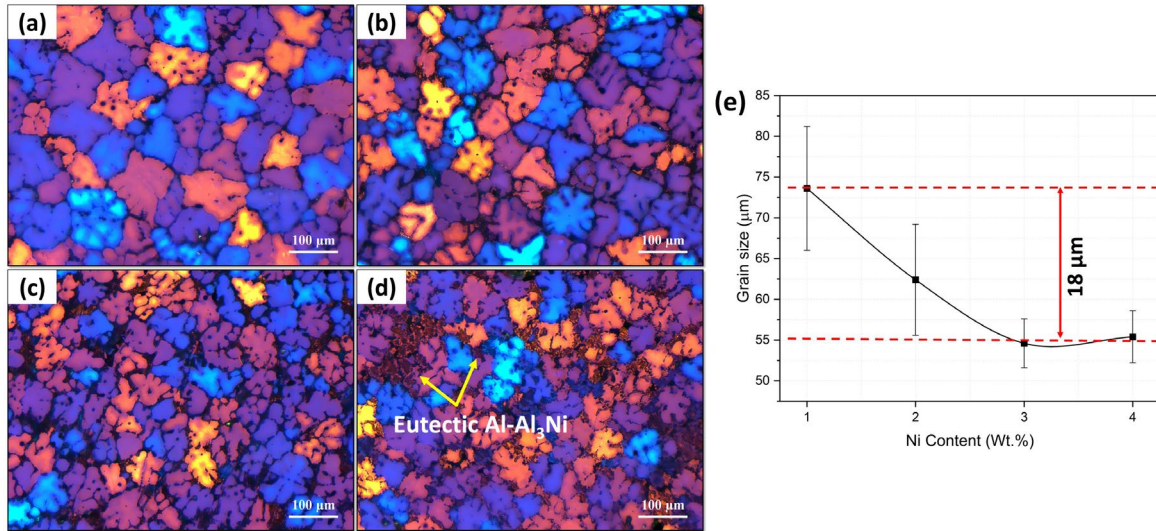
Figure 6. Typical grain structures shown in polarized optical micrographs for a) Al1Ni, b) Al2Ni, c) Al3Ni, and d) Al4Ni alloys; and (e) average grain size as a function of Ni content.

Figure 7 shows the microstructures of the four alloys obtained using OM and SEM. The microstructures of all the alloys comprised an α-Al matrix surrounded by a network of IMCs distributed mainly in the interdendritic region. The IMCs were characterized via SEM and EDS **(Figure 8)**. As shown by the SEM backscattered images in Figure 8, the different IMCs show different contrasts (i.e., white, grey, and black). Most of the IMCs (denoted by point A in Figure 8c) were eutectic Al_3Ni, which appeared white and exhibited a large and irregular plate-like shape. In addition, small and spherical Al(SiMgNi) intermetallic particles appearing in gray were distributed mainly in the α-Al matrix (denoted by point B). The result of EDS analysis indicates that this phase contained significant amounts of Si, Ni, and Mg (Fig. 8d). Moreover, a few Mg_2Si particles appearing in black (denoted by point C in Figure 8e) were observed in the interdendritic region. The area fractions of the various IMCs were quantitatively analyzed, and the results are presented in **Table 2**. As the Ni content increased, the proportion of eutectic Al-Al_3Ni increased; hence, the area fraction of Al_3Ni increased significantly. For instance, the area fraction of Al_3Ni increased from 6.16% to 28.24% as the Ni content increased from 1% to 4%. Notably, when the Ni content increased to 4%, most of the Al_3Ni intermetallic compounds became refined and appeared primarily as fine Al_3Ni particles in the eutectic Al-Al_3Ni structure, in addition to few, large and irregular plate-like Al_3Ni intermetallic particles (Figur 3d). The area fractions of both the Al(SiMgNi) and Mg_2Si intermetallics, as minor IMCs, did not change significantly with the Ni content in the alloys. After the solution treatment of T6, Al(Si,Mg,Ni) was dissolved completely, and most of the Mg_2Si particles disappeared from the microstructure (micrographs are not shown herein).
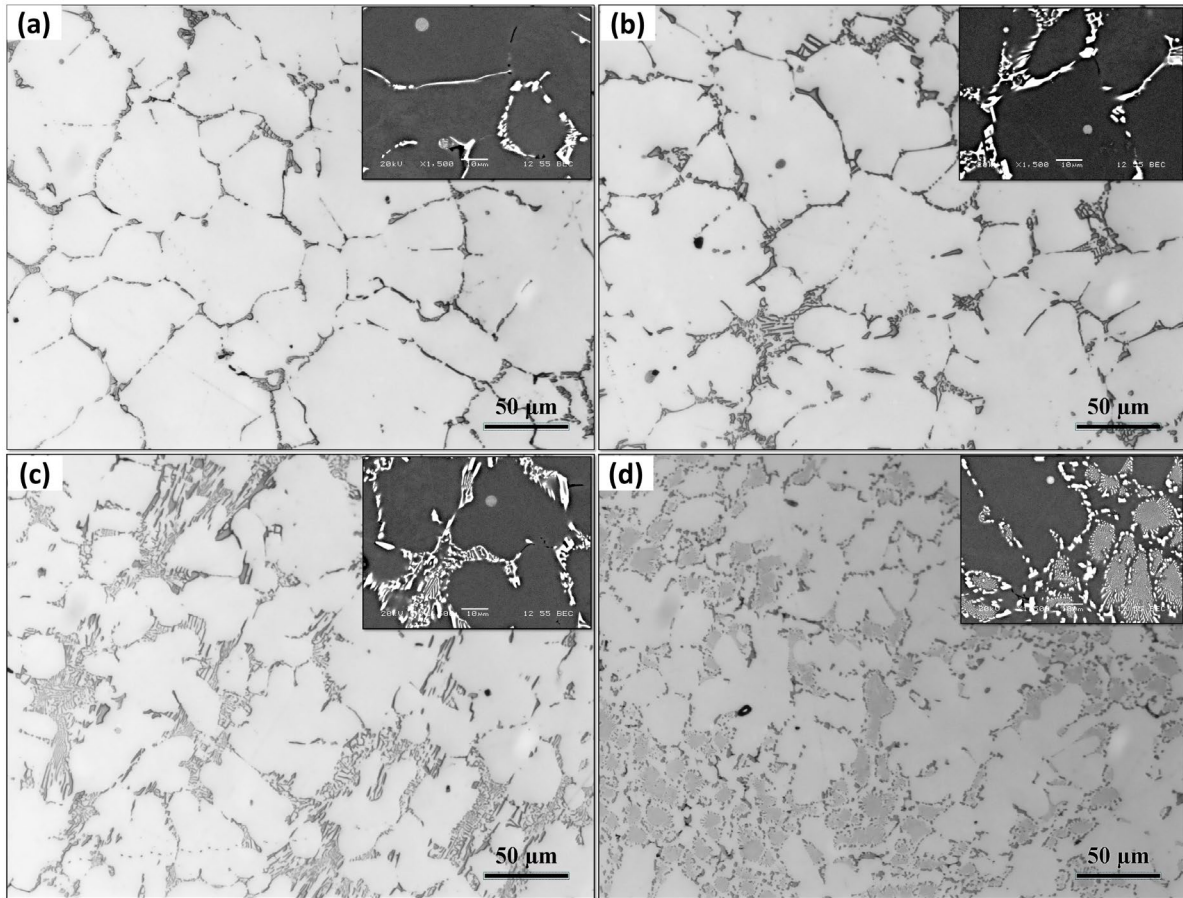
9

Figure 7. Optical micrographs showing distribution of IMCs in as-cast microstructures (a) Al1Ni, (b) Al2Ni, (c) Al3Ni, and (d) Al4Ni alloys. Inserted SEM backscattered images show distribution of IMCs.

Table 2. Quantitative results of different IMCs in the as-cast microstructure (vol.%)

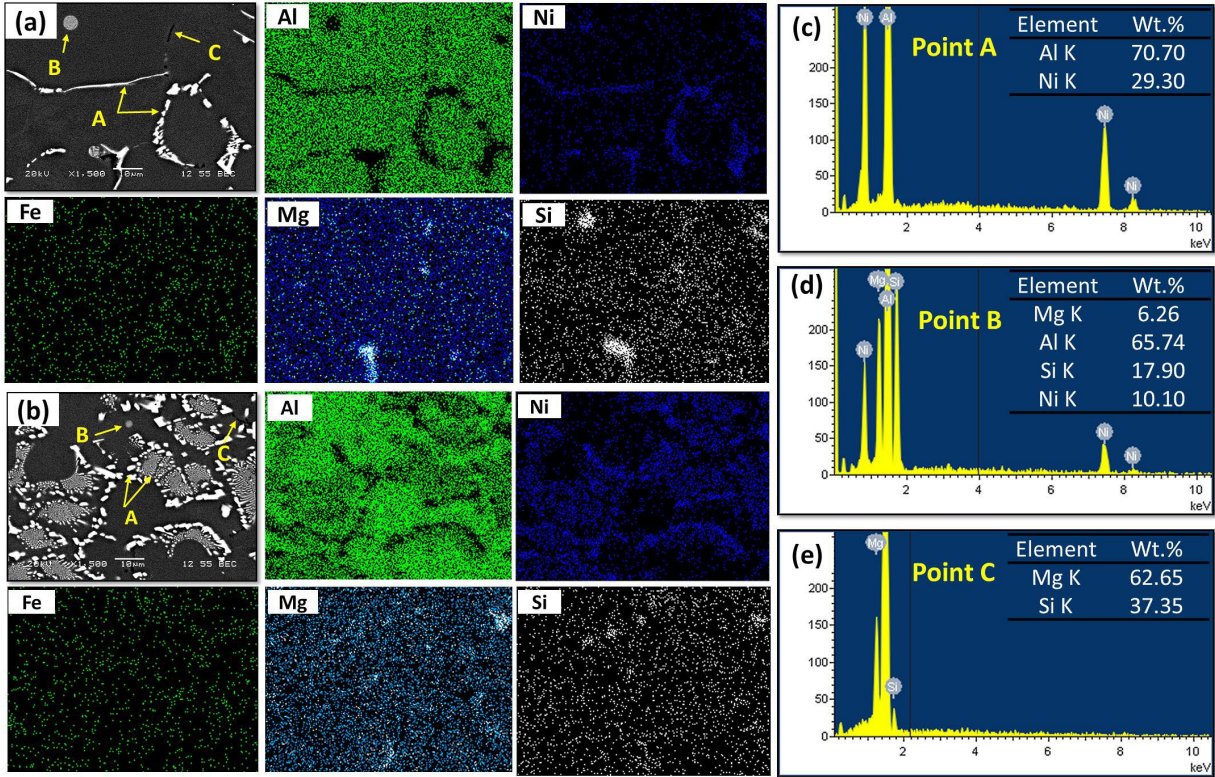|	Al_3Ni	Mg_2Si	Al(Si,Mg,Ni)	Total
Al1Ni	6.16±0.3	0.145±0.040	0.117±0.034	6.42
Al2Ni	10.38±0.8	0.163±0.043	0.118±0.032	10.66
Al3Ni	12.93±1.3	0.156±0.05	0.123±0.032	13.21
Al4Ni	28.24±2	0.143±0.04	0.117±0.026	28.50

Figure 8. SEM backscattered images and the corresponding EDS mapping analysis of various IMCs for (a) Al1Ni and (b) Al4Ni alloys; and EDS point analysis of each intermetallic phase represented as (c) point A, (d) point B, and (e) point C.

3.2.2 Evolution of precipitates during T5 and T6 treatments

Based on the strength and EC results (Figure 5), Al1Ni and Al4Ni alloys were selected for further microstructural observation via TEM. **Figure 9** shows the typical bright-field TEM micrographs, which reveal the evolution of precipitates in the α-Al matrix during both T5 and T6 treatments; the number densities of the precipitates are presented in **Table 3**. All the precipitations were MgSi-type precipitates, based on the TEM selected area diffraction patterns and information from the literature; they were classified based on size: β" (length ≤ 150 nm) and β' (length > 150 nm) [37, 38].

As shown in Figs. 9a and b, both alloys show a high number density of nanosized precipitates under the T5 condition. The Al1Ni alloy contained only β", whereas the Al4Ni alloys contained a mixture of β" and β' precipitates, where β" was predominant. The β" precipitates in the Al1Ni alloy were much finer and their number density was considerably higher than those in Al4Ni. In the Al4Ni alloy, two distinct precipitation regions were observed: (1) The matrix zone (MZ), which is the α-Al matrix where β"/β' precipitated and (2) the eutectic zone (EZ), which is the eutectic Al-Al₃Ni structure where β"/β' precipitated in the eutectic Al. As shown in Table 3, the β" precipitation, as the main strengthening phase, was significantly weaker in the EZ than in the MZ. However, the number density of β' precipitates was comparatively higher in the EZ than in the MZ.

Table 3. The number density of β" and β' precipitates (10^{-18} m^{-3}) after T5 and T6 treatments for Al1Ni and Al4Ni alloys.

	Al1Ni		Al4Ni			
			Matrix Zone		**Eutectic Zone**	
	β"	β'	β"	β'	β"	β'
T5	45267±4503	---	33805±1327	2293±96	9342±1347	4293±106
T6	71287±2365	2847±184	47741±1560	3221±381	17633±1536	6591±1740

Figures 9c-e show the β"/β' precipitation of both alloys in the T6 condition. In both alloys, a mixture of β" and β' was observed, in which β" predominated; the total number densities of β" and β' were significantly higher in the T6 condition than in the T5 condition. This is attributed to the highly supersaturated Mg and Si solutes in the matrix under the T6 condition, which is due to the dissolution of Al(Si,Mg,Ni) and Mg_2Si intermetallics during the high-temperature T6 solution treatment As shown in Figure 9c and Table 4, the Al1Ni alloy contained a higher amount of fine β" precipitates than the Al4Ni alloy. For instance, the number density of β" precipitates in Al1Ni was approximately $7.2 \times 10^{22}\ m^{-3}$ with a small amount of β' ($0.28 \times 10^{22}\ m^{-3}$), whereas alloy Al4Ni contained fewer β" ($6.5 \times 10^{22}\ m^{-3}$) but more β' ($0.98 \times 10^{22}\ m^{-3}$). The precipitation in the EZ of the Al4Ni alloy is shown in Figure 9e; as shown, the number density of β" precipitates ($1.8 \times 10^{22}\ m^{-3}$) reduced significantly, whereas β' precipitates almost doubled ($0.66 \times 10^{22}\ m^{-3}$) as compared with those in the MZ. In addition, a few large MgSi precipitates were observed in the EZ (Figure 9e), which were not homogeneously distributed around the Al$_3$Ni eutectic particles. The presence of these large precipitates is attributable to the quenching effect. Thermally induced dislocations are typically generated in the matrix during the quenching of the solution treatment owing to the thermal expansion mismatch between the matrix and intermetallic particles [39, 40]. The dislocation–Al$_3$Ni interfaces can provide heterogeneous nucleation sites for early MgSi precipitation in the EZ [41, 42].
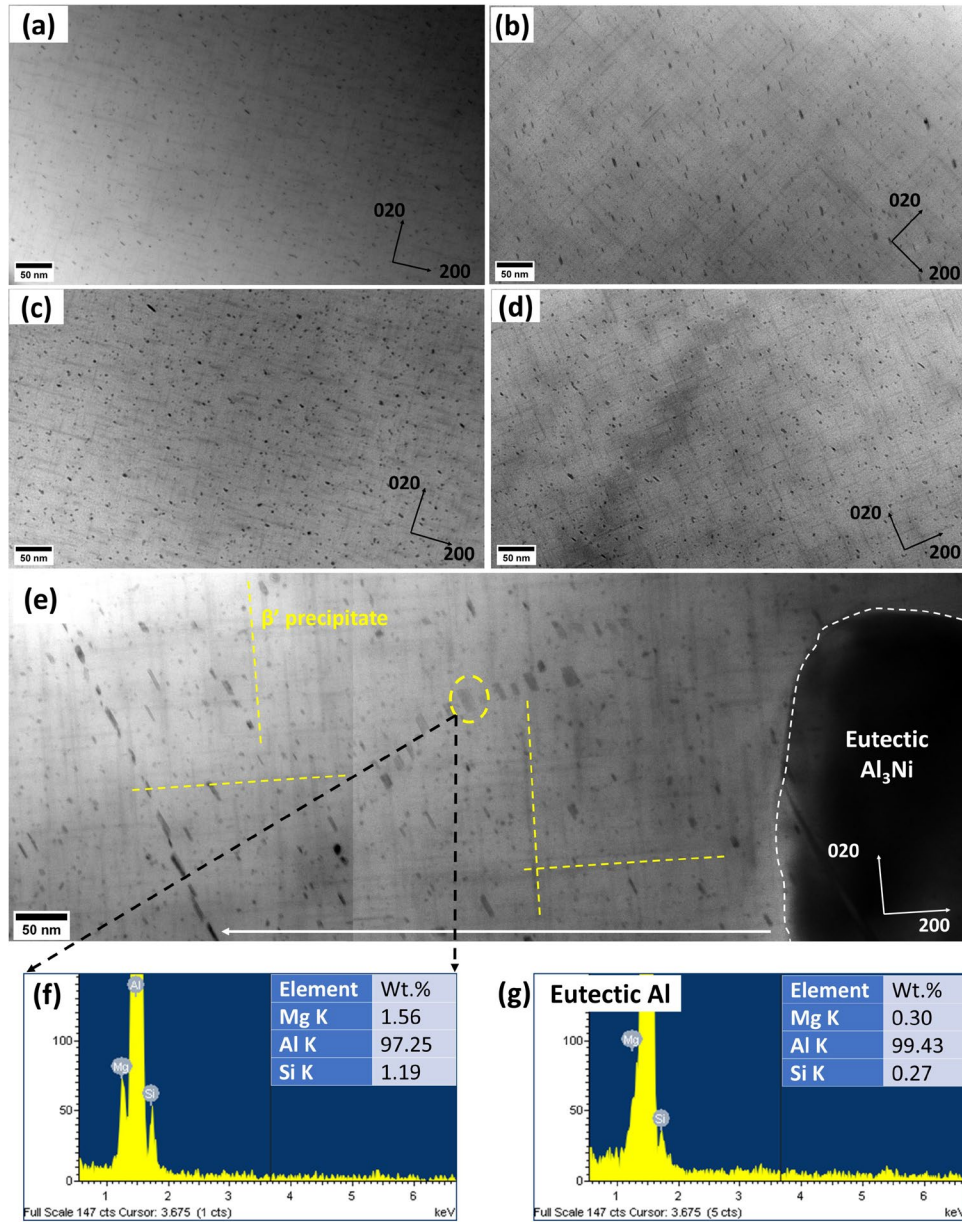
Figure 9. Bright-field TEM showing precipitation of β'' and β' in T5 condition (180 °C/12h) of (a) Al1Ni and (b) Al4Ni alloys; and in T6 condition (180 °C/24h) of (c) Al1Ni and (d) Al4Ni. (e) Precipitation in eutectic zone of Al4Ni. Representative TEM-EDS analysis (f) for seleected large precipitates and (g) eutectic Al matrix.

The eutectic Al_3Ni intermetallic in Al4Ni under both T5 and T6 conditions was observed via TEM, and the results are shown in **Figure 10**. Al_3Ni particles in the T5 condition (Figure 10a) remained unchanged and exhibited a rod-like morphology with a length exceeding 2 μm, as in the original as-cast condition. However, the eutectic Al_3Ni particles were fragmented and shortened (Figure 10b), with an average length of 250–800 nm under the T6 condition. The fragmentation of the Al_3Ni intermetallic was most likely caused by the high-temperature solution treatment of T6 because the aging temperatures of both T5 and T6 were not sufficiently high to induce such change.
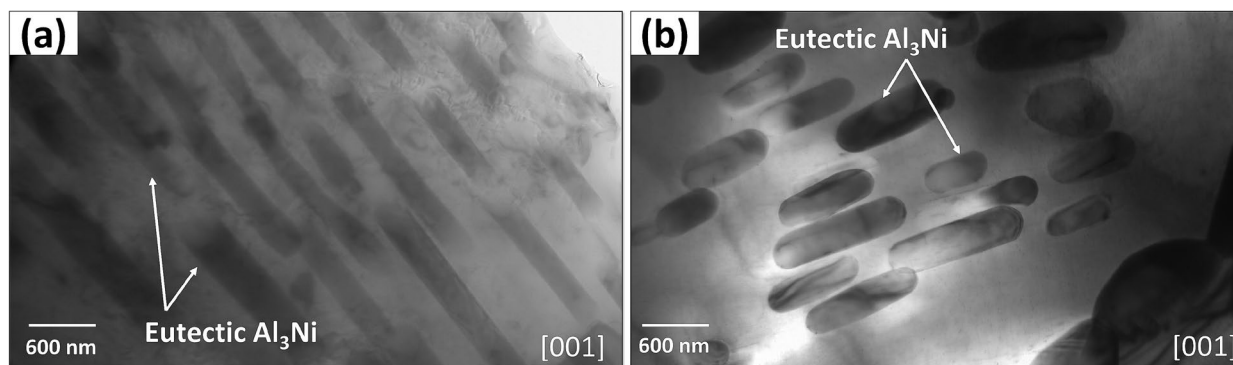
13

Figure 10. Bright-field TEM images showing morphology of eutectic Al₃Ni intermetallic in Al4Ni alloy under (a) T5 and (b) T6 conditions.

   A schematic illustration of the precipitation of β″ and β′ in the Al1Ni and Al4Ni alloys under the T6 condition is presented in **Figure 11**. The Al1Ni alloy contained primarily the α-Al MZ, whereas Al4Ni was composed of an MZ and EZ, where β″ and β′ precipitated in both zones. The precipitation behavior of β″/β' was correlated with the area fraction available for precipitation. The area available for precipitation of the Al4Ni alloy (71.8 vol.%) was considerably smaller compared with that of the Al1Ni alloy (93.8 vol.%). A smaller area fraction for precipitation results in higher concentrations of Mg and Si solutes, and hence a higher precipitation rate. Furthermore, eutectic Al₃Ni particles and thermally induced dislocations can accelerate the nucleation and growth of the precipitates [41-43]. Consequently, the precipitates in the Al4Ni alloy become coarser, and more β' precipitates are formed compared with those in the Al1Ni alloy. In particular, for the Al4Ni alloy, fewer β″ precipitates and more β' precipitates were observed in the EZ than in the MZ.
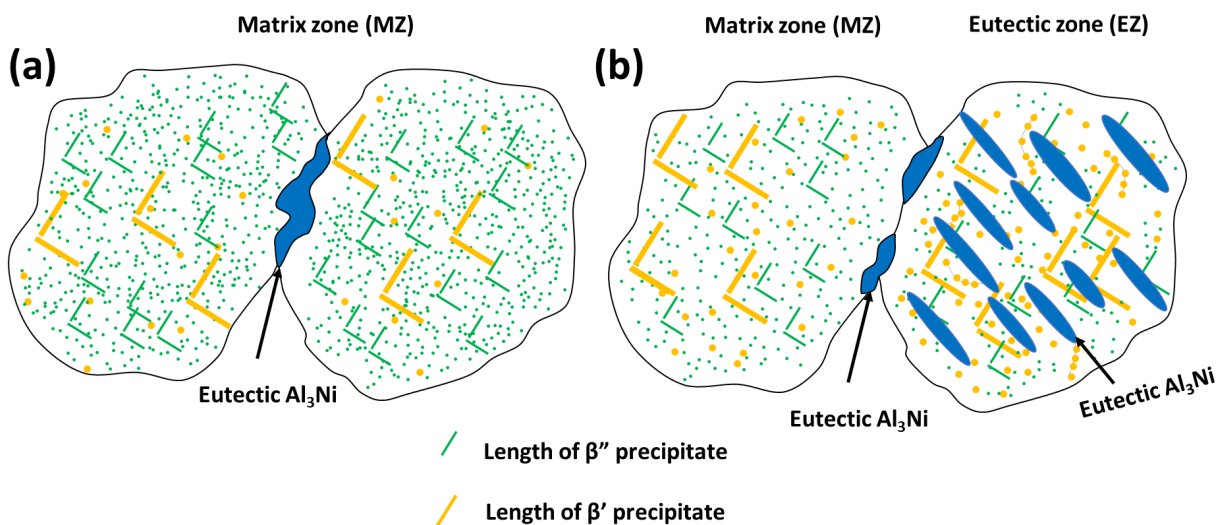

Figure 11. Schematic diagram showing precipitation of β″ and β' during T6 aging in (a) Al1Ni and (b) Al4Ni alloys.

3.3   Hot tearing susceptibility

Typical macro-images of the CRC mold castings of the four alloys are shown in **Figure 12**. The Al1Ni alloy was the most susceptible alloy to hot tearing, and complete fractures in the sample were observed in rods D and C, whereas a slight crack was observed in rod B (Figure 12a). As the Ni content increased, the hot-tearing resistance increased gradually. The Al2Ni sample exhibited large cracks in rods D and C, but no cracks in rod B (Figure 12b); meanwhile, large cracks in rod D and hairline cracks in rod C were observed in the Al3Ni alloy (Figure 12c). In the Al4Ni samples, only hairline cracks were observed in rods C and D (Figure 12d). The HTS indices of the four alloys were evaluated based on the severity of the macrocracks in the CRC-cast samples [33], and the results are presented in **Figure 13**. The HTS value decreased modestly from 84 in Al1Ni to 72 in Al2Ni, significantly decreased to 29 in Al3Ni, and further reduced slightly to 21 in Al4Ni. In general, Al1Ni and Al4Ni were the worst (HTS of 84) and best (HTS of 21) alloys, respectively, in terms of HTS.
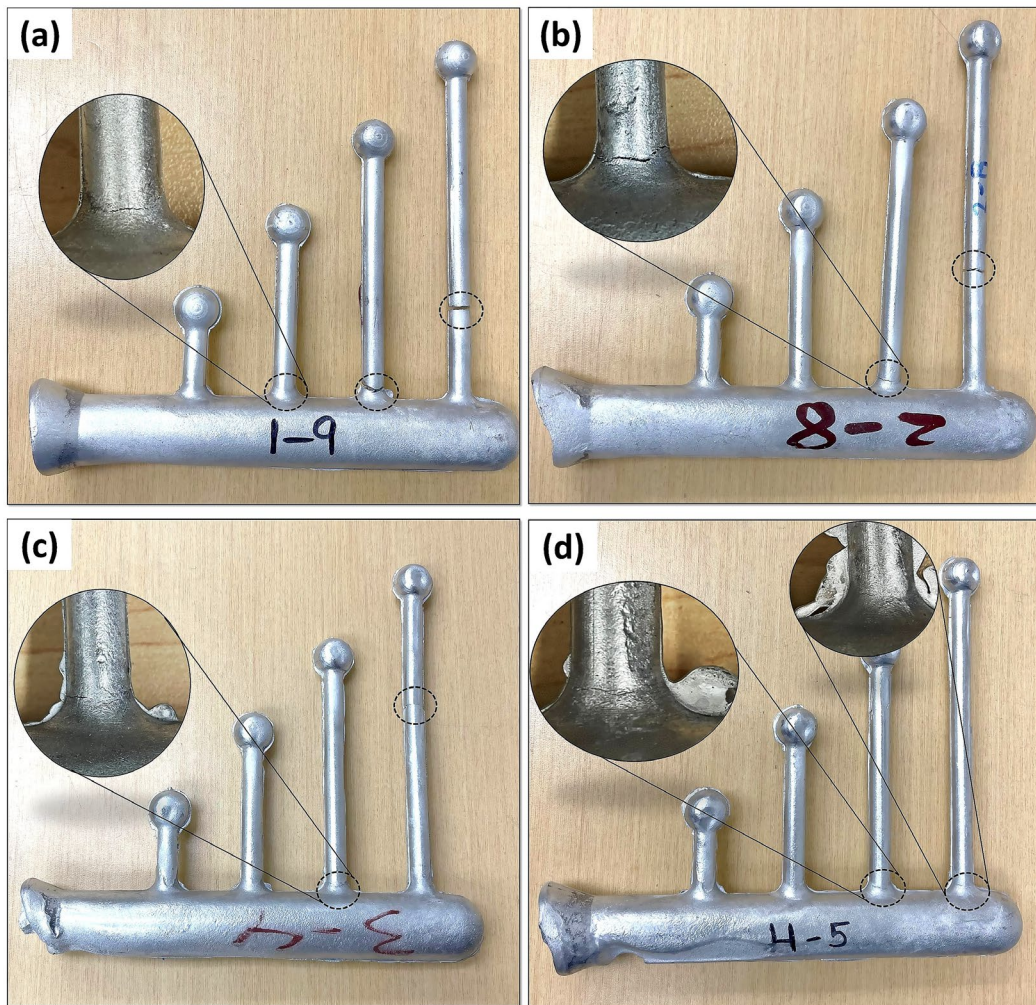

Figure 12. Castings for testing hot tears in Al-Ni-Mg-Si evaluated using CRC test mold: (a) Al1Ni, (b) Al2Ni, (c) Al3Ni, and (d) Al4(Ni).

Several models have been developed to predict the HTS of Aluminum alloys [31, 44, 45]. For example, Zolotorevskiy et al. [45] suggested a method of HTS prediction based on the calculation of the solidification range of the alloy (ΔT) using by Sheil model. In the present work, the solidification range of four investigated alloys has been calculated using ThermoCalc software based on Sheil model. The results show that the liquidus temperature slightly decreases with Ni, while the solidus temperature remains constant at 532.8 °C. The difference of ΔT between four alloys is quite small, which is hard to predict the HTS of this system. Moreover, Hu's model ($dT/d(f_s^{1/3})$ near $f_s^{1/3}$) [31] was developed recently and successfully applied to predict the HTS of samples with equiaxed grain structures. This criterion was based on the evolution of the solid fraction with temperature during the late stage of solidification, i.e., when hot tearing occurs primarily. The (T $vs.$ f_s ($f_s^{1/3}$)) curves for the four alloys were constructed based on thermodynamic calculations using the Scheil model, as shown in Figure 13b. Moreover, a solidification range of $0.92 < f_s < 0.99$ ($0.9753 < f_s^{1/3} < 0.9967$) was considered for this calculation [31, 44]. In addition, linear fitting was to validate with range, which indicated an R^2 value of 96%. The calculated hot tearing index ($\Delta T/\Delta f_s^{1/3}$) was imposed in Figure 13a, and it decreased gradually as the Ni content increased, which is consistent with the experimental HTS results.

The low HTS of the high-Ni alloys is attributable to two reasons. First, the grain size decreases as the Ni content increases (Figure 6), and the fine grains result in a uniform distribution of internal stresses during solidification, which reduces the likelihood of hot tearing [22, 25, 46]. Second, the increase in the eutectic Al-Al₃Ni portion in the microstructure with increasing Ni content (Figure 7) is favorable for reducing the HTS [1, 7, 29, 30]. Increasing the amount of eutectic Al-Al₃Ni, which presents excellent fluidity during the late stage of solidification, can mitigate HTS by re-heeling the initially formed tears.
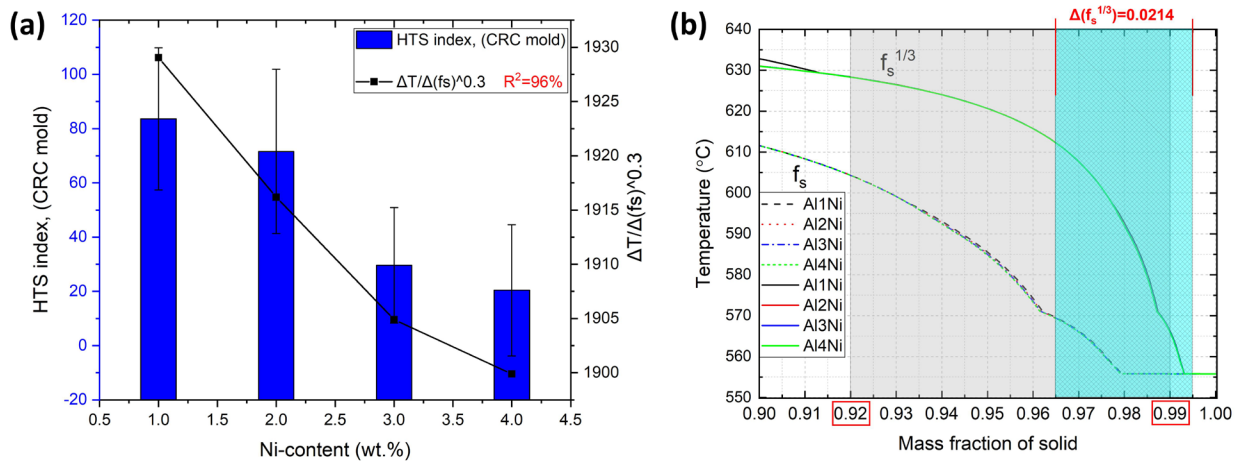

Figure 13. (a) Experimental HTS index from CRC samples and predicted hot tearing index ($\Delta T/\Delta f_s^{1/3}$), b) Prediction of hot tearing of Al-xNi-Mg-Si cast alloys based on $\Delta T/\Delta(f_S)^{1/3}$ in f_S range of $0.92 < f_s < 0.99$ ($\Delta f_s^{1/3} = 0.0214$).

4 Discussion

4.1 Correlation among EC, strength, and microstructure evolution

As shown in Figures 3 and 4, the EC and HV increased significantly during both the T5 and T6 treatments. The evolution of the EC and mechanical properties of the samples can be correlated with the microstructural evolution under as-cast and heat-treated conditions. As previously reported [11-13], any disruption in the crystal lattice periodicity (caused by structural defects, particularly by solute atoms) can deteriorate the EC.

The grain size (73.5 μm for Al1Ni alloy and 55 μm for Al3Ni and Al4Ni alloys) would give a negligible grain boundary contribution to electrical resistivity in the alloys with the different Ni contents. In addition, the dislocation density in an annealed aluminum is reported to be 10^{10}-10^{11} m^{-2} [34]. Therefore, the dislocation number densities are assumed to be insignificant in the as-cast and as-solutionized conditions, giving a negligible electrical resistivity contribution. Thus, the EC behaviors of the alloys during the aging are highly related to the solutes and precipitates [47]. It should be noted that the aging treatment would not affect the Ni solutes and intermetallics for each individual alloy. The extraction of the Mg and Si solutes from the matrix into the precipitates occurs during the aging. The precipitates cause a lower resistivity contributions than the Mg and Si solutes [14]. Accordingly, the precipitate formation led to enhance the EC with the aging time. Hence, this transition from Mg/Si solutes into Mg/Si precipitates plays a crucial role in increasing the EC during the aging treatment.

The EC decreased with the Ni content regardless of the aging temper (Fig. 5). This is attributed to the detrimental effect of the eutectic Al3Ni on the electron motion. The intermetallic compounds (Al3Ni) often have a different crystal structure and atomic arrangement compared to α-Al matrix. Therefore, the eutectic Al3Ni particles can create strong stress concentration within the aluminum matrix. Moreover, the eutectic Al3Ni particles cause less effective electron migration channels, leading to numerous interfaces and scattering the electrons. This scattering impact disturbs the flow of electrons and reduces the EC. Similar findings were observed for the eutectic Si in the Al-4Si-0.8Mg-0.6Fe alloy [48]. Accordingly, the Al1Ni alloy showed a higher EC at a given aging time in both T5 and T6 tempers (Fig. 5). However, the Al2Ni and Al3Ni alloys showed a similar EC behavior (Fig. 5), though the Al3Ni alloy has a higher Ni value than Al2Ni alloy. This could be correlated to the slightly higher Mg and Si contents in Al2Ni alloy relative to Al3Ni alloy, causing the slightly higher electrical resistivity [14]. Therefore, it resulted in a similar EC behavior in these two alloys (Al2Ni and Al3Ni).

Under the T5 condition, the tensile strength increased gradually with the Ni content (Figure 5). Although the number density of β" precipitates (as the main strengthening phase after T5) decreased slightly from Al1Ni to Al4Ni, the volume fraction of the Al3Ni intermetallic significantly with the Ni content, i.e., from 6.2 vol.% in Al1Ni to 28 vol.% in Al4Ni (Table 2). The eutectic Al3Ni intermetallic, which exhibited excellent properties (Young's modulus of 116–152 GPa and tensile strength of 2160 MPa), can provide additional strengthening to the Al-Ni system [49, 50]. Owing to the increased quantity of eutectic Al-Al3Ni in high Ni alloys, the

strengthening effect of the Al$_3$Ni intermetallic outweighs the effect of β'' precipitates; therefore, the Al4Ni alloy possesses the highest mechanical strengths in the T5 condition.

By contrast, the tensile strength decreased gradually as the Ni content increased under the T6 condition (Figure 5). The difference in the strength trend between T5 and T6 can be attributed to (1) the precipitation behavior of fine β'' precipitates in the matrix and EZs and (2) the area fraction of the α-Al matrix. Compared with the case under the T5 condition, the number density of β'' precipitates increased significantly (Table 3) owing to highly supersaturated Mg and Si solutes during the T6 solution treatment; hence, the strengthening effect of β'' was more prominent under the T6 condition. The amount of β'' precipitates decreased significantly as the Ni content increased owing to the reduced α-Al matrix. For instance, the number density of β'' reduced from 7.1×10^{22} m^{-3} in Al1Ni to 4.7×10^{22} m^{-3} in Al4Ni. In addition, the amount of β'' precipitates in the α-Al matrix was higher than that in the EZ of the high-Ni alloys. Therefore, as the Ni content increased, the strengths (YS and UTS) decreased in high Ni alloys, and the Al4Ni alloy with the highest Ni content exhibited the lowest mechanical strength under the T6 condition.

4.2   Overall performance in terms of castability, EC and strength

To determine the overall performance of Al conductor-cast alloys, three critical properties, i.e., the EC, strength, and castability, should be considered and optimized. **Figure 14** shows a comparison of the critical properties (i.e., EC, YS, and HTS) of the four alloys investigated, alongside the minimum targeted EC (48% IACS) [3]. The four Al-Ni-based alloys can be categorized into two groups based on their HTS: (1) a high HTS group for low-Ni alloys (Al1Ni and Al2Ni), which are not suitable as castable alloys, and (2) a low HTS group for high-Ni alloys, including Al3Ni and Al4Ni, as appropriate cast alloys. The Al4Ni alloy in the low-HTS group exhibited the lowest HTS and excellent mechanical properties (HTS of 21 MPa; and YSs of 205 and 246 MPa under T5 and T6, respectively). However, the EC of this alloy did not satisfy the minimum targeted value of 48% IACS, which implies that conductor alloys fabricated using this alloy would not achieve the desirable electrical properties.

Meanwhile, decreasing the Ni content of the Al3Ni alloy to 3% considerably improved the EC to values above the minimum target value (i.e., 49.4% IACS and 49.7% IACS under T5 and T6, respectively), and the HTS value was slightly higher than that of the Al4Ni alloy. In general, the Al3Ni alloy demonstrated better balance among the HTS, EC, and YS, and its comprehensive performance under T5 and T6 conditions (HTS of 29, EC of ~ 49.5% IACS, YS of 178 MPa in T5, and 251 MPa in T6) were better than those of the other three experimental alloys investigated; thus, it is preferable for the fabrication of Al conductor cast alloys.

The Al3Ni alloy under the T5 condition was an excellent medium-strength conductor cast alloy, with an EC of 49.4% IACS and a YS of 178 MPa. Performing T5 direct aging without T6 treatment may be promising in industrial practice because (1) the distortion of the cast component owing to quench-induced thermal stresses during the solution treatment of T6 can be prevented and (2) the high-temperature T6 solution treatment can be eliminated in terms of the cost effectiveness. In this regard, the Al4Ni alloy under the T5 condition can be an alternative medium-strength conductor cast alloy with a slightly low EC of 47.8% IACS but a superior YS of 205 MPa.

However, for high-strength conductor alloys, T6 treatment is necessary to achieve a high strength level (e.g., Al3Ni-T6) via maximizing the strengthening effect of β″ precipitates through Mg and Si microalloying in Al-Ni-based alloys.
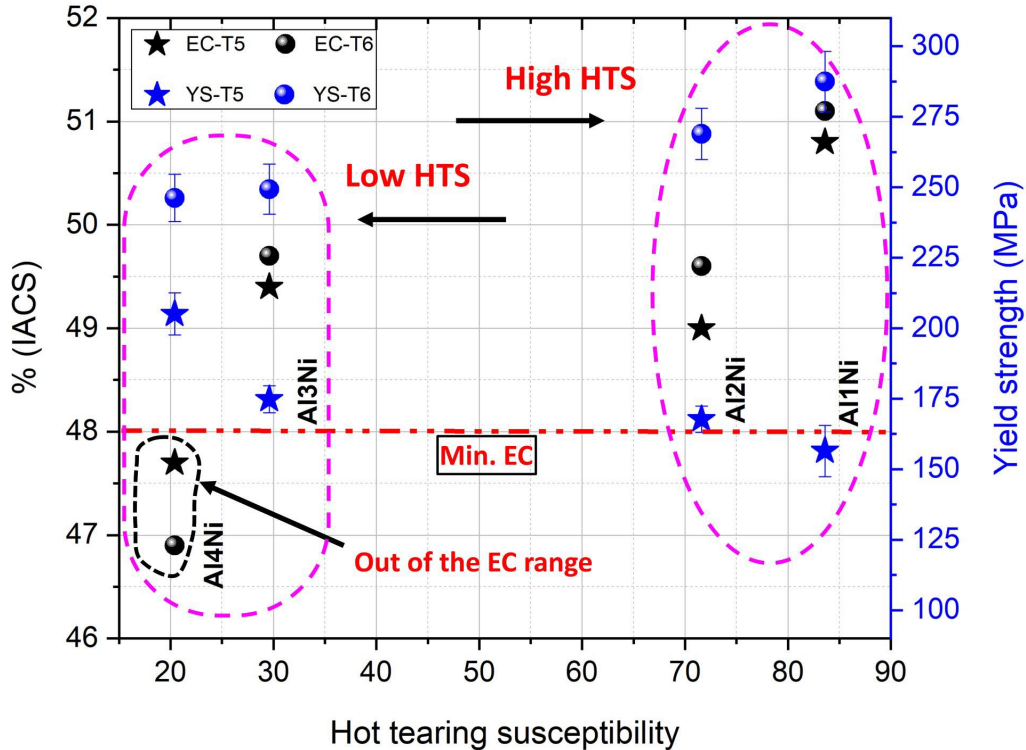

Figure 14. Comparison of three critical properties, i.e., EC, strength, and HTS, for the four alloys investigated. Dashed red line shows minimum targeted EC for Al conductor cast alloys.

4.3   Comparison of current YS and EC values with those in literature

Figure 15 shows a comparison of the YS and EC values of the experimental alloys obtained in this study with data available from the literature pertaining to Al-cast alloys [2, 3]. Based on the critical EC value of 48% IACS, the alloys can be classified into low- and high-EC alloys. As shown in Figure 15a, commercial 356-T6 and 317-T7 alloys generally exhibit excellent castability and superior strength but significantly low ECs (< 40% IACS), which do not satisfy the minimum EC requirement for electric vehicle components. Among the high-EC alloys (Figure 15b), four alloys in the literature (Al-1Si-0.5Mg, Al-1Si-0.4Ni-0.03Ti, Al-3.6Si-0.4Mg-0.03Ti-T5, and Al-5.1Ni) and three alloys in this study (Al1Ni-T5, Al2Ni-T5, and Al3Ni-T5) satisfy the critical EC for medium-strength alloys (YS of 150-200 MPa). Among these alloys, three alloys, i.e., Al-1Si-0.5Mg, Al-1Si-0.4Ni-0.03Ti, and Al-3.6Si-0.4Mg-0.03Ti-T5, are expected to experience severe HTS; Al-5.1Ni is expensive because of its high Ni content. Therefore, the Al3Ni-T5 alloy in this work, with its low HTS and high YS, render it the best medium-strength conductor cast alloy.

Among the high-strength alloys (see Fig. 15b, YS of 250–300 MPa), three alloys in this study (Al1Ni-T6, Al2Ni-T6, and Al3Ni-T6) outperformed all the other existing alloys. As mentioned

above, the Al3Ni-T6 alloy with excellent comprehensive performance (low HTS, high EC, and high YS) is the most promising candidate for high-EC and high-strength conductor-cast alloys.
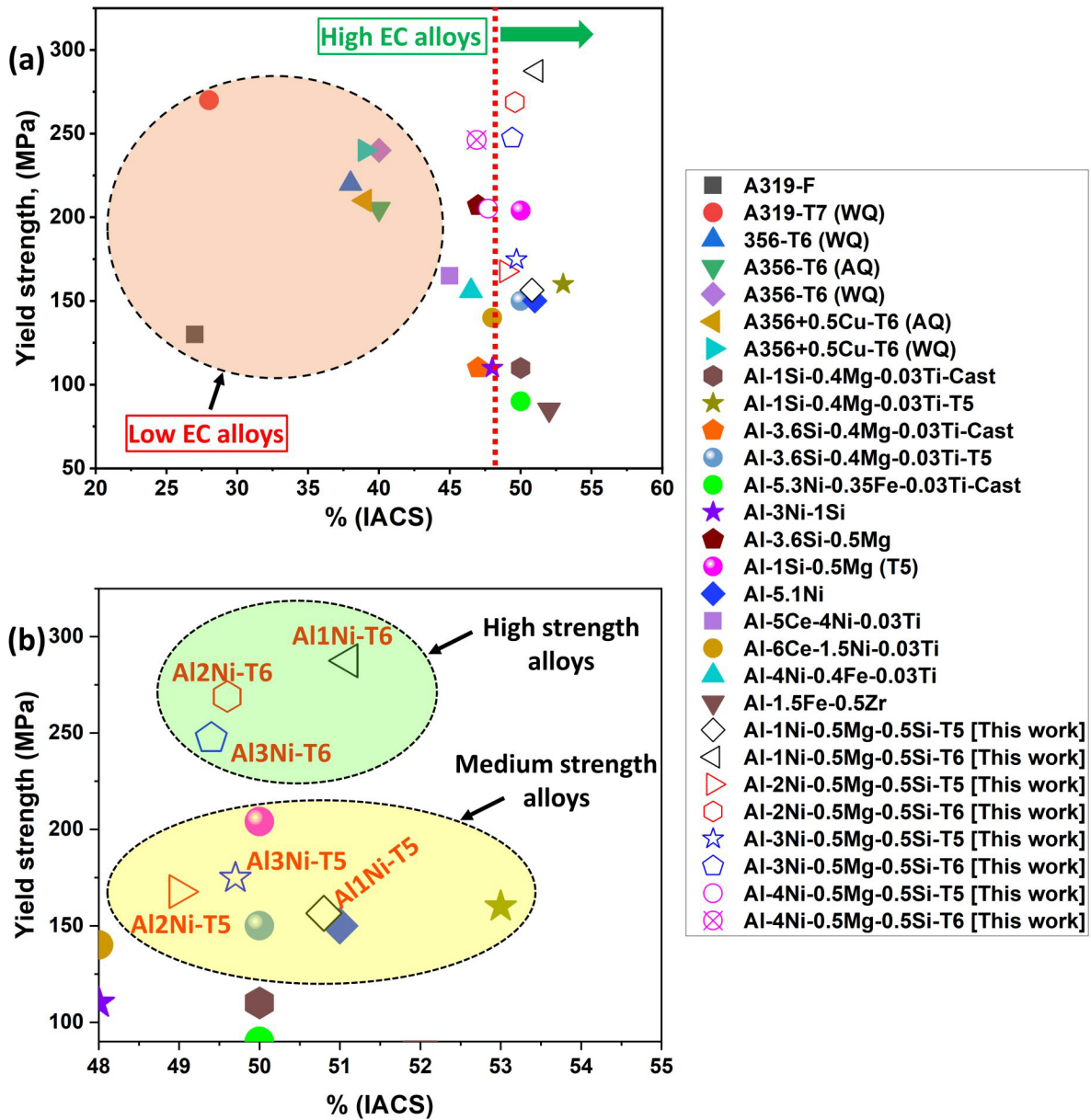

Figure 15. Comparison of YS and EC values of various Al cast alloys (a); enlarged view of high-EC alloys for Al-based conductor cast alloys (b).

5   Conclusions

1. The cast microstructures of all alloys comprised an α-Al matrix surrounded by Al_3Ni and Mg_2Si intermetallic particles along the interdimeric region. As the Ni content increased, the quantity

20

of eutectic Al-Al$_3$Ni increased; hence, the volume fraction of the eutectic Al$_3$Ni intermetallic increased significantly. All the alloys comprised equiaxed grains, and their grain sizes decreased as the Ni content increased.

2. By adding Mg and Si into the Al-Ni-based alloys, numerous β"/β' precipitated in the α-Al matrix and eutectic Al after T5 and T6 treatments, thus significantly improving the EC and mechanical strength. Under the T5 condition, the tensile strength increased gradually with the Ni content, whereas the opposite was observed under the T6 condition.

3. By increasing the Ni content from 1% to 4%, the HTS reduced significantly, mainly because of the increased amount of eutectic Al-Al$_3$Ni and the decrease in the grain size. The Al3Ni and Al4Ni alloys indicated low HTS, which renders them suitable for the fabrication of castable conductor alloys. Hu's model ($dT/d(f_s^{1/3})$ near $f_s^{1/3}$) was applied to predict the HTS index, and the results were consistent with the HTS experimental results.

4. In terms of comprehensive performance – low HTS, high EC and superior YS – the Al3Ni alloy containing 0.55Mg-0.55Si outperformed three other experimental alloys investigated and achieved excellent EC and YS values of 49.4% IACS and 178 MPa under the T5 condition, respectively, and 49.7% IACS and 250 MPa under the T6 condition, respectively, while exhibiting a low HTS. Thus, this alloy is preferable for the fabrication of Al conductor cast alloys.

Declaration of Competing Interest

The authors declare that they have no known competing financial interests or personal relationships that could have appeared to influence the work reported in this paper.

Data Availability Statement

The data that support the findings of this study are available from the corresponding author upon reasonable request.

References

[1] F. Liu, X. Zhu, S. Ji, *J. Alloys Compd.* 2020, 821, 153458.

[2] S. Palanivel, C. Kuehmann, J.R. Stucki, E. Filip, P.K. Edwards, Aluminum alloys for die casting, International Patents Application No., US2021/0332461A1.

[3] P. Sivanesh, K. Charlie, S. Robert, F. Ethan, E. Paul Aluminum alloys for die casting, International Patent Application No. WO 2020/028730 A1.

[4] S. Kotiadis, A. Zimmer, A. Elsayed, E. Vandersluis, C. Ravindran *Metall. Mater. Trans. A* 2020, 51, 4195-4214.

[5] T. Koutsoukis, M.M. Makhlouf Int. J. Met. 2016, 10, 342-347.

[6] J.-M. Kim, H.-S. Yun, J.-S. Park, K.-T. Kim, *Int. J. Cast Met. Res.* 2014, 27, 141-145.

[7] J.-M. Kim, N.-H. Kim, K.-T. Kim, S.-H. Ko, Mater. Res. Innov. 2015, 19, S8-460-S8-463.

[8] J.F. F. Breton, M. Morel *Die Casting Congress & Tabletop, North American Die Casting Association* 2019.

[9] Y. Han, D. Shao, B. Chen, Z. Peng, Z. Zhu, Q. Zhang, X. Chen, G. Liu, X., Li *J. Mater. Sci.* 2017, 52, 4445-4459.

[10] S. Jiang, R. Wang, JMST 2019, 35, 1354-1363.

[11] S.N. Khangholi, M. Javidani, A. Maltais, X.G. Chen, J. Mater. Res. 2022, 37, 670-691.

[12] X. Sauvage, E. Bobruk, M.Y. Murashkin, Y. Nasedkina, N. Enikeev, R. Valiev, *Acta Mater.* 2015, 98, 355-366.

[13] Q. Zhao, Z. Qian, X. Cui, Y. Wu, X. Liu, *J. Alloys Compd.* 2016, 666, 50-57.

[14] S.N. Khangholi, M. Javidani, A. Maltais, X.-G. Chen, J. Mater. Res. 2020, 35, 2765-2776.

[15] K. Hilpert, D. Kobertz, V. Venugopal, M. Miller, H. Gerads, F. Bremer, H. Nickel *Zeitschrift für Naturforschung A* 1987, 42, 1327-1332.

[16] E. Karakulak, F.G. Koç, R. Yamanoglu, M. Zeren *Materials*, *Mate. Test.* 2016, 58, 117-121.

[17] P. Sankanit, V. Uthaisangsuk, P. Pandee, *J. Alloys Compd.* 2021, 889, 161664.

[18] A. Ilbagi, P.D. Khatibi, H. Henein, R. Lengsdorf, D. Herlach, J. Phys.: Conference Series, IOP Publishing, 2011, 012010.

[19] H. Kaya, U. Böyük, E. Çadırlı, N. Maraşlı, *Mater. Des.* 2012, 34, 707-712.

[20] Y. Cho, H. Kim, W. Kim, D. Jo, J. Lee, *Mate. Today: Proceedings* 2015, 2, 4924-4930.

[21] M.A. Easton, H. Wang, J. Grandfield, C.J. Davidson, D.H. StJohn, L.D. Sweet, M.J. Couper, *Metall. Mater. Trans. A* 2012, 43, 3227-3238.

[22] D. Eskin, L. Katgerman, *Prog. Mater. Sci* 2004, 49, 629-711.

[23] M. Uludağ, R. Cetin, D. Dispinar, *Metall. Mater. Trans. A* 2018, 49, 1948-1961.

[24] H. Hyer, L. Zhou, A. Mehta, S. Park, T. Huynh, S. Song, Y. Bai, K. Cho, B. McWilliams, Y. Sohn *Acta Mater.* 2021, 208, 116698.

[25] Y. Li, H. Li, L. Katgerman, Q. Du, J. Zhang, L. Zhuang, *Prog. Mater. Sci* 2021, 117, 100741.

[26] J. Elambasseril, M.J. Benoit, S. Zhu, M.A. Easton, E. Lui, C.A. Brice, M. Qian, M. Brandt, Prog. Addit. Manuf. 2022, 7, 887–901.

[27] S. Li, D. Apelian, K. Sadayappan Int. J. Met. 2012, 6, 51-58.

[28] A.S. Sabau, B.K. Milligan, S. Mirmiran, C. Glaspie, A. Shyam, J.A. Haynes, A.F. Rodriguez, J. Gonzalez Villarreal, J. Talamantes *Metals* 2020, 10, 430.

[29] A. Nabawy, A. Samuel, H. Doty, F. Samuel, Int. J. Met. 2021, 15, 1362-1374.

[30] J.A. Taylor, *Prog. Mater.* 2012, 1, 19-33.

[31] B. Hu, Z. Li, D. Li, T. Ying, X. Zeng, W. Ding, *JMST* 2022, 105, 68-80.

[32] S.M. Allen, *Philos. Mag.* 1981, A 43, 325-335.

[33] G. Razaz, T. Carlberg, *Metall. Mater. Trans. A* 2019, 50, 3842-3854.

[34] S.N. Khangholi, M. Javidani, A. Maltais, X.-G. Chen, Mater. Sci. Eng. A 2021, 820, 141538.

[35] C. Liu, J. Chen, Y. Lai, D. Zhu, Y. Gu, J. Chen, Mater. Des. 2015, 87, 1-5.

[36] M. Easton, D. StJohn, *Metall. and Mater. Trans. A* 1999, 30, 1613-1623.

[37] S. Andersen, H. Zandbergen, J. Jansen, C. TrÆholt, U. Tundal, O. Reiso, *Acta Mater.* 1998, 46, 3283-3298.

[38] K. Teichmann, C. Marioara, S. Andersen, K. Pedersen, S. Gulbrandsen-Dahl, M. Kolar, R. Holmestad, K. Marthinsen, *Philos. Mag.* 2011, 91, 3744-3754.

[39] R. Arsenault, N. Shi, Mater. Sci. Eng. A 1986, 81, 175-187.

[40] M. Taya, K. Lulay, D. Lloyd, Acta Metall. Mater. 1991, 39, 73-87.

[41] C. Wu, K. Ma, D. Zhang, J. Wu, S. Xiong, G. Luo, J. Zhang, F. Chen, Q. Shen, L. Zhang, Sci. Rep. 2017, 7, 1-11.

[42] T. Hu, K. Ma, T. Topping, J. Schoenung, E. Lavernia, *Acta Mater.* 2013, 61, 2163-2178.

[43] M.V. Canté, J.E. Spinelli, N. Cheung, A. Garcia, Met. Mater. Int. 2010, 16, 39-49. 39-49.

[44] S. Kou, *Acta Mater.* 2015, 88, 366-374.

[45] A. Pozdniakov, V. Zolotorevskiy *Int. J. Cast Met. Res.* 2014, 27, 193-198.

[46] S. Li, D. Apelian *International*, Int. J. Met. 2011, 5, 23-40.

[47] S.N. Khangholi, M. Javidani, A. Maltais, X.-G. Chen, *J. Alloys Compd.* 2022, 914, 165242.

[48] X. Cui, H. Ye, H. Liu, X. Li, Q. Man, H. Li, H. Cui, R. Feng, Y. Pan, *J. Alloys Compd.* 2023, 938, 168275.

[49] J. Hernandez-Sandoval, G. Garza-Elizondo, A. Samuel, S. Valtiierra, F. Samuel, Mater. Des. 2014, 58, 89-101.

[50] H.T. Naeem, K.S. Mohammed, K.R. Ahmad, A. Rahmat , Adv. Mater. Sci. Eng. 2014, vol. 2014.